LASER & PHOTONICS REVIEWS
www.lpr-journal.org

On-Chip Broadband Multiwavelength Microlaser Array in Visible Region

Lilong Ma, Hongkun Zhong, Tao Yang, Leiying Ying, Jinhui Chen, Zhan Su, Shaoqiang Chen, Guoen Weng, Yang Mei,* and Baoping Zhang**

On-chip integrated microlaser sources are critical components in silicon (Si) photonics, which has become one of the leading photonic integrated circuits (PICs) technologies due to low cost, eco-friendly, large-scale integration and inherent compatibility for complementary metal-oxide-semiconductor (CMOS) manufacturing processes. Until now, however, it still remains a significant challenge to achieve an active microlaser with a quality factor of up to 10^4 and heterogeneous integration of multiple broadband wavelength-tunable microlasers for Si-based PICs. Here, a scalable strategy is reported to realize simultaneous integration of multiwavelength GaN-based microdisk laser arrays on Si(100) substrates. The microlaser exhibits a high-quality factor of 13 138 and a low threshold density of 57.85 μJ cm^{-2}. By precisely modulating the microdisk size and/or shape and thus the corresponding cavity loss, the lasing wavelength can be dynamically tuned over a large spectral range from 455 to 503 nm, which is physically unraveled by the gain profile shifting for different threshold energy levels conditions. This study opens a new path toward the realization of on-chip integrated broadband multiwavelength laser sources for Si-PICs platform, where only an epi-wafer and a single round of wafer bonding processes are needed.

1. Introduction

With global data traffic boosting, the electrical interconnects are no longer sufficient to meet the demands of high-speed, energy-efficient, and cost-effective data transmission in present data centers and high-performance computing systems. In recent years, silicon (Si) photonics is emerged as a key technology to mitigate the "inter-connect bottleneck" in data processing and transmission.[1] Building photonic integrated circuits (PICs) on an industry-standard Si wafer holds distinct advantages in high-speed performance, high integration density, and low power consumption.[2] In particular, Si photonics are inherently compatible with complementary metal-oxide-semiconductor (CMOS) manufacturing and packaging technologies, which allows for scalable and low-cost production of PICs on 200 or 300 mm wafers. Nowadays, Si-based PICs have also received increasing interest in other various applications such as quantum communication,[3] light detection and ranging,[4] microwave engineering,[5] metrology,[6] and bio/chemical sensing,[7] etc. At the heart of the Si-PIC platform is the on-chip laser source. However, due to the intrinsic nature of indirect bandgap of Si material, realizing a compact, energy-efficient, and robust on-chip laser source on Si is the key challenge for Si photonics. Although group IV material-based Ge and Ge-alloy (GeSi and GeSn) lasers on Si,[8] as well as Si Raman lasers have been developed by strain and band structure engineering,[9] the laser performances are still far behind the requirements for practical applications. Alternatively, integrating group III-V materials on Si substrates is widely considered as the most promising pathway toward developing on-chip lasers. III-V materials are direct bandgap semiconductors with a substantially higher emission efficiency and optical gain than indirect bandgap materials. Various integration strategies have been developed for III–V/Si platform, including hybrid integration,[10] heterogeneous integration based on wafer bonding,[11] and monolithic integration based on direct epitaxial growth.[12] Recently, highly reliable wafer scale lasers have been demonstrated with a threshold of <2 mA and a lifetime of >100 years by using monolithic epitaxial grown GaAs-based quantum dot on Si.[13]

L. Ma, H. Zhong, T. Yang, L. Ying, J. Chen, Y. Mei, B. Zhang
Laboratory of Micro/Nano-Optoelectronics
Department of Micro Electronic and Integrated Circuits
Xiamen University
Xiamen 361005, China
E-mail: meiyang@xmu.edu.cn; bzhang@xmu.edu.cn

Z. Su, S. Chen, G. Weng
State Key Laboratory of Precision Spectroscopy
Department of Electronic Engineering
East China Normal University
500 Dongchuan Road, Shanghai 200241, China
E-mail: egweng@ee.ecnu.edu.cn

G. Weng
State Key Laboratory of Materials for Integrated Circuits
Shanghai Institute of Microsystem and Information Technology
Chinese Academy of Sciences
865 Changning Road, Shanghai 200050, China

B. Zhang
Institute of Nanoscience & Applications
Southern University of Science and Technology
Shenzhen 518055, China

The ORCID identification number(s) for the author(s) of this article can be found under https://doi.org/10.1002/lpor.202500151

DOI: 10.1002/lpor.202500151

Among various kinds of on-chip light sources for Si-PICs, broadband multi-wavelength laser array (MWLA) with multiple wavelength channels integrated on a single chip are attracting considerable attention because of their great potential for applications in multi-channel optical communication and computing networks,[14] spectroscopy, sensing of multiple biomarkers, and wavelength selective optical switching.[15] For example, in coherent wavelength division multiplexing optical communication networks, multi-channel laser sources with different wavelengths are required for flexible wavelength allocation and extending channel capacity.[16] In 2022, optical transceivers with a capacity of 800 G are demonstrated by integrating an 8-channel transmitter with 100 Gbps modulators and on-chip distributed feedback (DFB) MWLAs.[17] Different strategies have been explored to achieve the photonic integrated MWLAs. Grating-based tunable MWLAs, including the DFB laser arrays and the distributed Bragg reflector (DBR) type vertical-cavity surface-emitting laser (VCSEL) arrays, are the most developed and commercially available. The lasing wavelengths can be allocated by varying the grating Bragg wavelength from laser to laser in the array. On the other hand, whispering-gallery-mode (WGM)-based microlasers with in-plane emission have also attracted considerable attention for their potential as compact and low-threshold coherent light sources for densely integrated photonic circuits.[18] According to WGM resonant condition $2\pi Rn_{eff} = m\lambda$, where R is microdisk radius, n_{eff} is the effective index, m is the longitudinal mode number and λ is the resonant wavelength, an MWLA can be realized by varying the microdisk radius. Over the past decades, 4-channel, 5-channel, and 16-channel WGM-based MWLA have been realized by carefully controlling the cavity size.[19] However, the spectral coverage of those MWLAs is usually in the order of 20–30 nm, limiting the possible channel number and bandwidth. Different gain materials can be attached to the lasers to extend the wavelength by using, for example, transfer printing techniques or multi-turn wafer bonding.[20] Nevertheless, these approaches will inevitably increase the complexity of material growth and device fabrication processes. Furthermore, the reported on-chip MWLAs are almost all based on InP and GaAs materials working in original band and conventional band above the Si bandgap, and the on-chip MWLA in visible region is still rare.

Extending Si photonics into the visible spectrum can increase the integration density and bring Si-PICs to an even wider range of emerging applications, including on-chip visible light communication with huge bandwidth resources,[3a,21] spectroscopy and flow cytometry,[22] neurophotonics,[23] underwater communication,[24] scanning displays,[25] and augmented/virtual reality (AR/VR).[26] In the near ultraviolet to red spectral region, III-nitride-based semiconductors including GaN, AlGaN, and InGaN are ideal choices to fabricate visible on-chip lasers due to their wide direct bandgap and high luminescence efficiency.[27] As a core unit of the visible Si-PICs, however, the research about on-chip III-nitride-based visible lasers is still limited. In 2016, Sun et al. reported the first continuous-wave (CW) electrically injected GaN-based blue-violet laser directly grown on Si,[28] and they later realized GaN-based DFB lasers monolithically grown on Si in 2022.[29] However, high-quality GaN-based material can only be epitaxially grown on Si(111) substrates, which is not compatible to the current CMOS process. To realize GaN-based visible lasers on CMOS-compatible Si(100), substrate peeling together with nitride film transfer and bonding techniques have been developed, and a variety of nitride-based lasers have subsequently been demonstrated on Si(100), including Fabry-Pérot (FP) lasers,[30] VCSELs,[31] WGM lasers, [32] and photonic crystal (PC) lasers.[33] However, the broadband visible on-chip MWLAs, which are of great significance for real-world applications, have rarely been reported.

In this study, we report a unique and efficient method for the heterogeneous integration of GaN-based microdisk MWLAs on Si(100) substrate covering a wide spectral range from 455 to 503 nm. The MWLA with different lasing wavelengths is based on the same InGaN gain material, and the on-chip integration of the laser array is realized by a single round of wafer bonding, which is much simplified compared to the counterparts for GaAs systems. The fabricated GaN-based microdisk lasers have a "mushroom" configuration, showing low lasing threshold under optical pumping and a high Q-factor of 13 138 for GaN-based microcavity lasers. The utilized InGaN quantum well (QW) active region presents an intrinsic tunable gain spectrum depending on pumping energy levels due to both the screening of the quantum-confined Stark effect (QCSE) and the band-filling effect. By integrating cavities with different losses, multi-channel of lasers with different thresholds can be easily fabricated on a single chip through lithography and other conventional semiconductor processes. The cavity loss for each device can be precisely modulated by controlling the microdisk size and shape, resulting in a controllable lasing threshold for respective devices. The dissimilarity in threshold pump levels denotes the different degrees of material gain shift among various devices, leading to the distinct lasing wavelength for individual microdisks. Our results provide a very promising approach to realize single-chip multi-wavelength laser sources in visible region for Si-based PIC platforms.

2. Results and Discussion

In this work, GaN microlaser arrays were fabricated using a single transfer technique, as depicted in **Figure 1a** (The Experimental Section). Figure 1b shows the top-view scanning electron microscope (SEM) images of the prepared microdisk arrays with different shapes, and Figure 1c shows part of the enlarged inclined-view SEM image near the peripheral area of the circular microdisk. The air gap under the microdisk can be clearly observed. The atomic force microscope (AFM) image of the microdisk surface is shown in Figure 1d with a root-mean-square (RMS) roughness of ≈0.29 nm on a 10 × 10 μm^2 area. The microdisk was thinned and polished by chemical mechanical polishing(CMP), so that the GaN defect-rich layer was removed and a flat microdisk surface was obtained. The optimized substrate transfer technique plays an important role in reducing the scattering loss during light oscillations.[32a]

The optical properties of the InGaN MQW wafer with high Indium content were first probed by using a micro-photoluminescence (μ-PL) and time-resolved PL (TRPL) measurement system at room temperature. Detailed information of the measurement system is given in Section S1 (Supporting Information). **Figure 2a** shows the excitation-energy-dependent PL spectra of the InGaN MQW wafer. With increasing excitation energy, the light output exhibits a single peak at ≈526 nm at

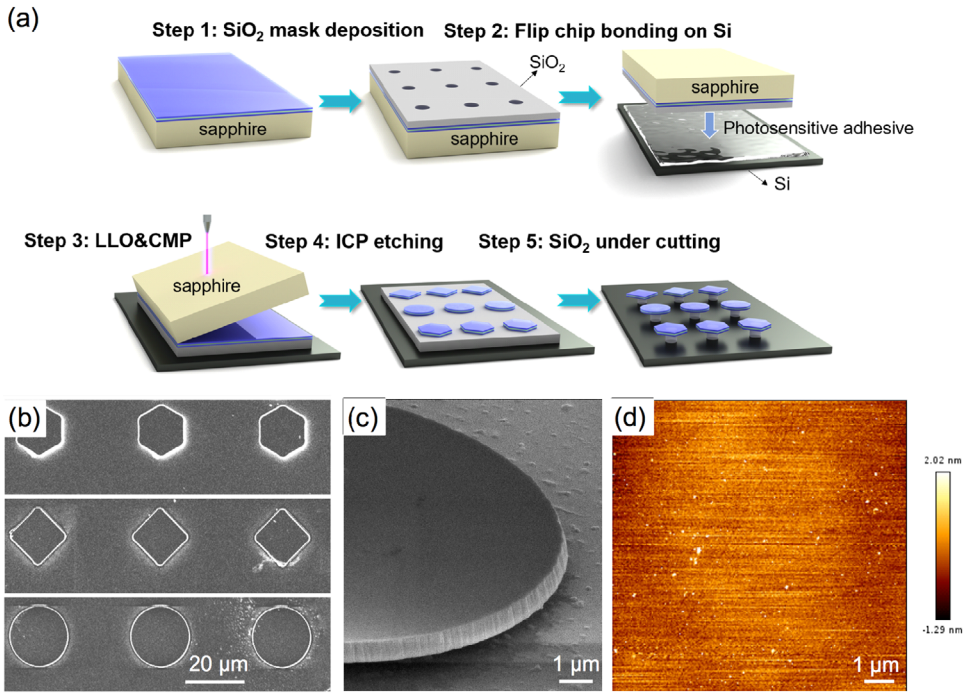

Figure 1. a) Fabrication processes of GaN-based microdisk MWLAs on Si(100). b) Top-view SEM images of microdisk arrays with different shapes. c) Enlarged inclined-view SEM image near the edge area of the circular microdisk. d) AFM image of the GaN-based microdisk surfaces.

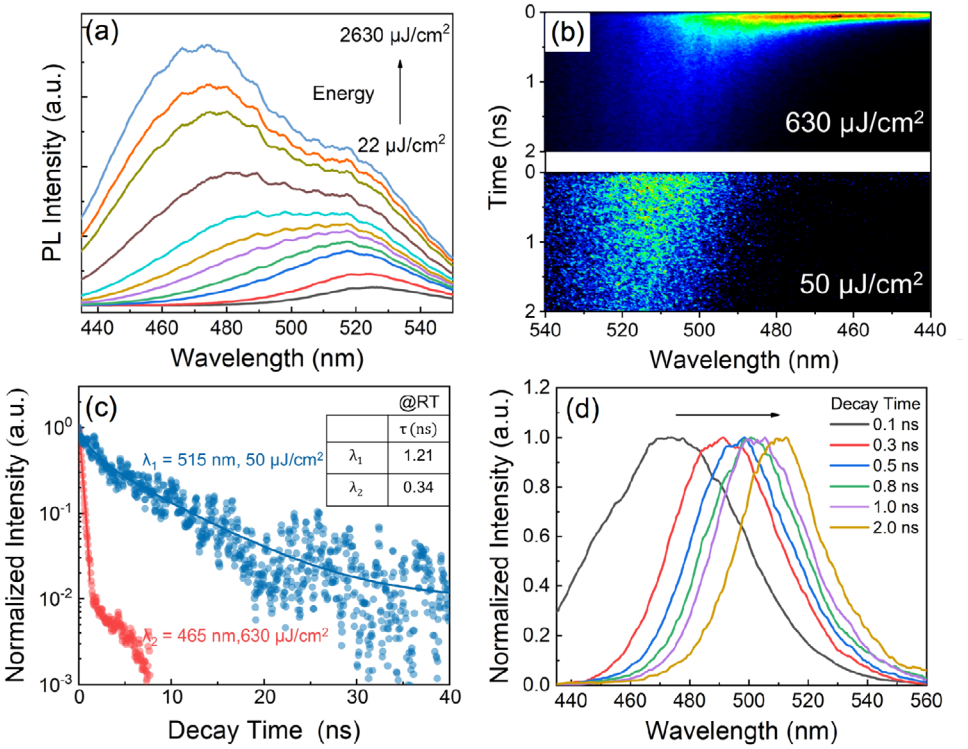

Figure 2. a) PL spectra of the InGaN MQW wafer. b) Streak-camera images of epitaxial wafer at various excitation energy. In the vertical dimension, a time range of 2 ns for each slice is shown. c) TRPL curves and fitting results at 465 and 520 nm wavelengths. d) Temporally resolved PL spectra with varying time delays for epitaxial wafer at 630 μJ cm^{-2}.

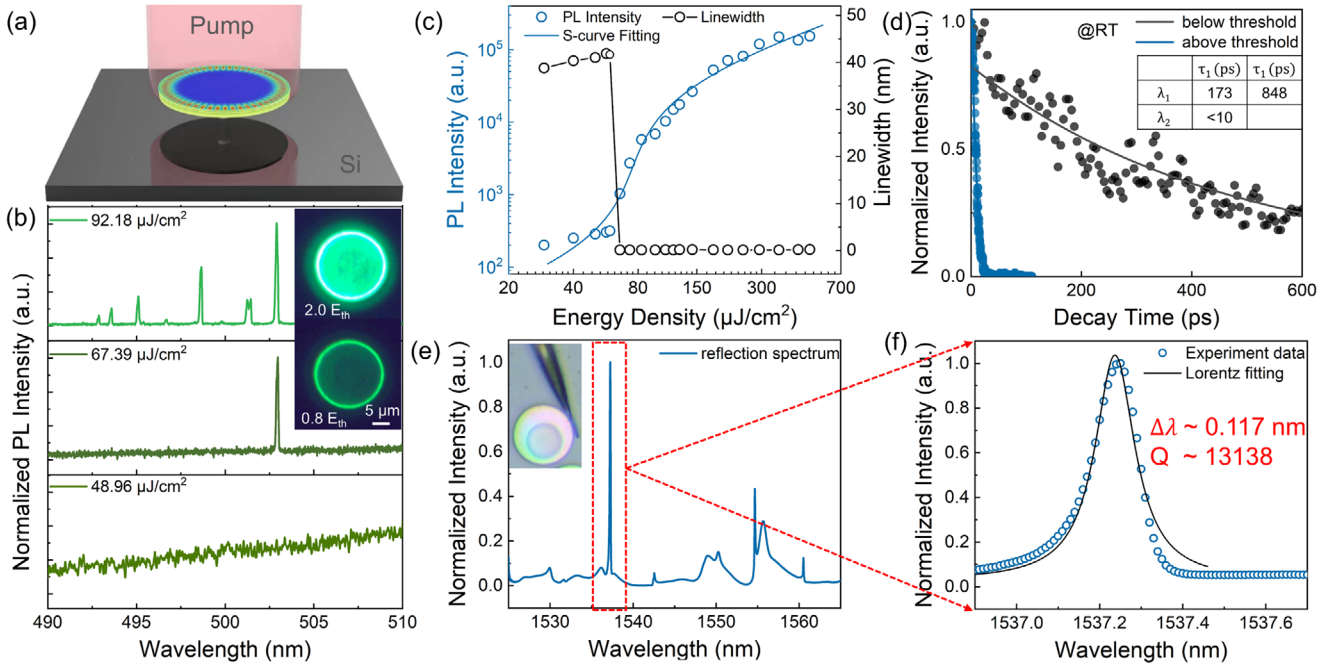

Figure 3. a) Schematic diagram of a microdisk under optical pumping. b) Normalized PL spectra at different pump energies. The illustration in (b) shows PL test system schematic and the luminescence diagram of the microdisk below and above the threshold. c) The emission intensity as well as the linewidth as a function of excitation energy. d) TRPL curves and fitting results below and above the threshold. e) The reflection spectrum of the microdisk with a diameter of 20 μm. The inset shows a microscopy image of the microdisk and the tapered fiber. f) Diagram of the Q factor, implying a high Q factor of 13 138 according to the Lorentz fitting curve.

first and then undergoes a large blueshift with a new emerging high-energy peak at 473 nm. The full width at half maximum (FWHM) of the spectra also increased from 40 to 104 nm. The large blueshift and spectral broadening under high injection level is peculiar to InGaN QWs with high Indium content, which is caused by both the screening of the quantum confined Stark effect (QCSE) and the band filling effect.[34] The new emerging peak at high energy is a sign of transition from the excited states in the QWs, and it can be further declared by the TRPL results shown in Figure 2b. With the increase of pump energy from 50 to 630 μJ cm^{-2}, the emission peak of the TRPL image at the initial stage just after the transient excitation shifted from 515 to 465 nm. From a fitting analysis, the decay time of the high energy peak at 465 nm is 0.34 ns, much shorter than the 1.21 ns for the low energy peak at 515 nm, as shown in Figure 2c. Note that the TRPL curve of the peak at 465 nm was extracted from the data under high excitation energy of 630 μJ cm^{-2}, since the signal at 465 nm is nearly undetectable under low excitation energy (50 μJ cm^{-2}). The short lifetime of the high-energy emission is evidence of the transition from the excited states, which can be explained by the larger overlap between electron and hole wavefunctions and the fast carrier relaxation from excited states to ground states. Figure 2d shows the spectral evolutions of the InGaN MQW wafer with a different time delay after the transient excitation at 630 μJ cm^{-2}. As the decay time increases, the carriers at high energy levels drastically decrease due to the rapid radiative and non-radiative recombination as well as the carrier relaxation from the excited state to the ground state, resulting in continuous redshifts of the center wavelength. The broad and tunable material gain of InGaN-based MQWs can support lasing at different wavelengths through modulating the gain profile, and have great potential in fabricating the MWLAs with a wide spectral range.

Figure 3a depicts the schematic diagram of a microdisk under optical pumping. Figure 3b shows the normalized PL spectra of an individual circular microdisk with a diameter of 20 μm at different pumping levels. At low pumping energy, the microdisk exhibits a broad spontaneous emission spectrum. When the pump energy reaches the threshold, a sharp laser emission at ≈503 nm is clearly observed. As the pump energy further increases, multiple-order WGM lasing occurs due to the mode competition within the microcavity.[35] The insets of Figure 3b display the fluorescence microscopy images of the circular microdisk below and above the threshold, respectively. Figure 3c shows the emission intensity and the linewidth as a function of excitation energy. The typical "S" shape output behavior and abrupt reduction of the linewidth prove unambiguously the lasing action. The threshold energy density and the corresponding transient threshold power density are 57.85 μJ cm^{-2} and 57.85 kW cm^{-2}, respectively. To get additional insights into the lasing dynamics, we performed TRPL measurements of the microdisk at different pumping energies, as shown in Figure 3d. The fitting result reveals a fast decay time of 173 ps and a slow decay time of 848 ps at low pump energy below the threshold. When the pump energy exceeds the threshold, the carrier lifetime sharply decreases to less than 10 ps (resolution limit) due to the ultrafast transition of stimulated emission, further confirming the lasing behaviors. The Q factor of the microdisk was also measured under a "cold cavity" condition by coupling a superluminescent diode (SLD) source to the cavity through tapered fiber and collecting the reflection spectrum. Detailed informa-

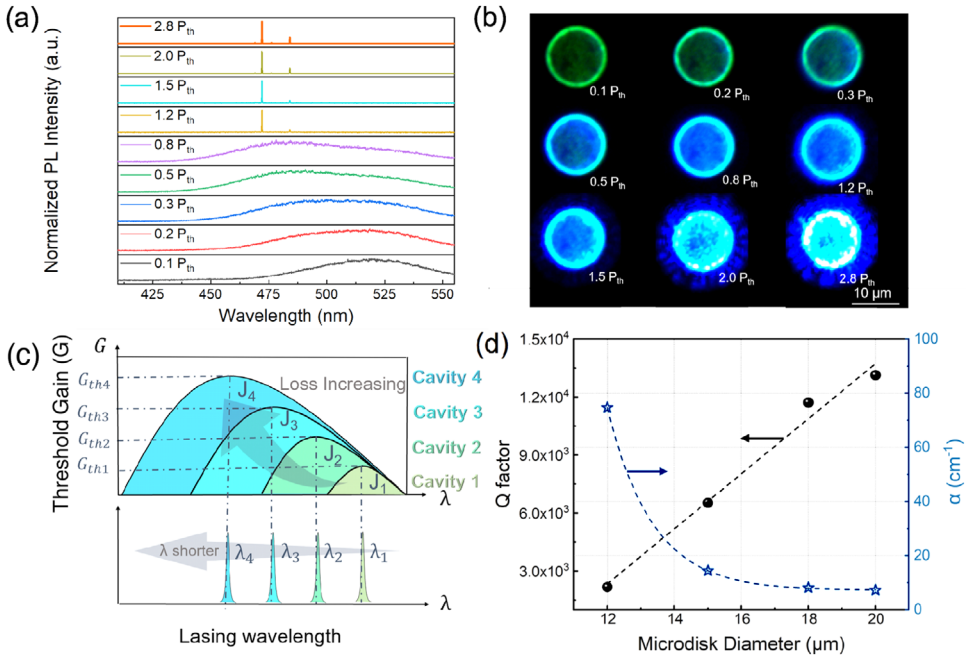

Figure 4. a) Normalized PL spectra for circular microdisks with a diameter of 12 μm. b) Luminescence diagram of the circular microdisk under the corresponding pumping conditions. c) Physical model for cavity-loss-related lasing mode variation. d) Q factor and α of microdisks with diameters of 20, 18, 15, and 12 μm, respectively.

tion of the measurement system is given in Section S2 (Supporting Information). The normalized reflection spectrum is shown in Figure 3e. The Lorentzian fitting of the reflection spectrum shows a linewidth of 0.117 nm at a wavelength of 1537.2 nm, corresponding to a Q factor as high as 13 138, as shown in Figure 3f. Such a high Q factor for the widely-reported GaN-based microcavity lasers should benefit from the high-quality GaN film and the smooth microdisk morphology, as shown in Figure 2. The cavity Q factor evaluation was conducted in the 1.55 μm band instead of the green lasing band, which is determined by the emission wavelength of the SLD for Q measurement setup. This can exclude the light absorption by the active region, thereby enabling the evaluation of cavity loss under a "cold cavity" condition. The Q factor of the microdisk at the visible region was also measured by directly fitting the PL spectra below lasing threshold and turned out to be 10 263. Detailed information is given in the Section S3 (Supporting Information).

The microdisk with a diameter of 20 μm shows lasing action in the green spectral region, however, it is found that a cavity with a smaller diameter can lase at a much shorter wavelength by using the same InGaN MQWs with broad tunable gain spectrum. **Figure** 4a displays the variation of PL spectra with a diameter of 12 μm under progressively higher excitation fluences, and Figure 4b shows the corresponding luminescence microscopic image. Below lasing threshold, only featureless spontaneous emission in the green region was obtained, while the spectral center gradually shifts toward shorter wavelength from green at 525–475 nm which locates at blue region with the increase of pumping energy, being in consistent with the luminescence microscopic images. When the pump fluence increases beyond the threshold, a distinct lasing peak at 473 nm appears. We can clearly observe the WGM modes at the periphery of the microdisk, with blue edge emission dominating the overall output. Note that the mechanism of the large blueshift in a smaller cavity is very different from the commonly reported size-induced resonant wavelength shift due to the quantum confinement or strain relaxation effect.[36] In our scenarios, however, it is the carrier-density-related band-filling effect and the screening of the QCSE that play dominant roles in determining the optical gain profile and thus the lasing wavelength. The free spectral range (FSR) of a 12 μm GaN-based microdisk here is ≈1.2 nm, much smaller than the linewidth of the gain profile. In principle, multiple modes in a resonant cavity are competitive with each other, and the one with the highest gain will dominate.[37] Therefore, the lasing wavelength of the microdisk is determined by the maximum point of the gain profile when pumping reaches a threshold, which can be clearly revealed by the proposed physical model in Figure 4c. Note that the lasing threshold of the 12-μm microdisk is 145 μJ cm^{-2}, ≈2.5 times higher than that of the 20-μm one. This can be attributed to the larger cavity loss in a smaller cavity due to its higher sensitivity on cavity sidewall defects and the larger mode leakage.[11a] The gain spectrum shows a large blueshift with increasing pumping energy, and finally lasing was realized at a much shorter wavelength. In other words, by modulating the cavity losses to variate the lasing threshold, different lasing wavelengths can be obtained from the microdisks with broad tunable optical gain.

By controlling lasing wavelength through cavity loss modulation for respective microdisks, it has great potential to realize the on-chip MWLA. The concept and corresponding physical model are schematically shown in Figure 4c. Cavities with different losses have different threshold gain G_{th}. As the microdisk losses increase, G_{th} is increased accordingly, and then higher pump energy is required to achieve lasing action. Since the higher carrier

injection level will lead to a blueshift of gain spectrum of InGaN MQWs with high indium content, when the maximum material gain equals to G_{th}, lasing is consequently realized at a shorter wavelength for the cavity with higher-level loss. It is important to highlight that the significant blue shift in the gain spectrum as excitation intensity increases occurs only under pumping conditions below the lasing threshold. It should be noted that the large spectral blueshift of gain spectrum with increasing excitation intensity occurs only under the pumping conditions below lasing threshold. Once lasing takes over, the rapid consumption of carriers through stimulated emission leads to an almost constant carrier density in active regions with increasing excitation energy. This stabilization of carrier density prevents further band filling. Therefore, heterogeneous integration of MWLA on Si(100) substrate can be realized by fabricating multi-cavities with different losses. The most direct method to modulate microdisk cavity losses is to change the cavity size. We fabricated the circular GaN-based microdisk MWLA with various diameters on Si(100) substrate using the same InGaN MQW wafer and carried out the Q factors by the tapered fiber reflectance measurement system. Q factor can reflect the oscillation loss within the cavity according to the relationship:[38]

$$Q^{-1} = \frac{\alpha\lambda}{2\pi n_{eff}} \tag{1}$$

where the loss coefficient α is the total loss, n_{eff} is the effective refractive index of the medium, and λ is the mode wavelength. The loss of each part is refined into the following relationship:

$$\frac{1}{Q} = \frac{1}{Q_{rad}} + \frac{1}{Q_{abs}} + \frac{1}{Q_{scats}} \tag{2}$$

where the $\frac{1}{Q_{rad}}$ is the microcavity radiation loss, $\frac{1}{Q_{abs}}$ is the internal absorption loss and $\frac{1}{Q_{scats}}$ is the scattering loss. For microcavities larger than a few microns, low radiation losses can usually be achieved. The absorption loss is given as:[39]

$$\frac{1}{Q_{abs}} \cong \frac{2\lambda\gamma\omega}{\pi c\left(1 - \frac{1}{n_{eff}^2}\right)D} \tag{3}$$

where γ is the absorption rate of a material consisting entirely of that at the microdisk edge surface, ω is the width of the surface absorbing layer, D is the diameter of the microdisk, c is the velocity of light. The material scattering loss is given as:[39–40]

$$\frac{1}{Q_{scat}} \cong \frac{16\pi^{\frac{5}{2}}\left(n_{eff}^2 - 1\right)hL_C\sigma_R^2}{3\lambda^3 D} \tag{4}$$

where h is the thickness of the microdisk, L_C is the length related to the roughness of the side wall of the microcavity, σ_R is the standard deviation of the roughness amplitude. It can be seen that the decrease of the microcavity diameter will lead to a decrease of the Q value and an increase of the loss. Figure 4d shows the Q factor and losses of microdisks with diameters of 20, 18, 15, and 12 μm, respectively. The detailed reflection spectra are given in the supplementary information Figure S1 (Supporting Information). It is seen that the Q factor decreased from 13 138 to 2180 when the diameter of the microdisks decreased from 20 to 12 μm. The loss is approximately inversely proportional to the diameter of the microdisk, which is consistent with the above theory. Particularly, small cavities are more sensitive to cavity sidewall defects and exhibit larger mode leakage. This suggests the larger losses and threshold energies in smaller microdisks, as well as the feasibility of loss modulation through cavity-size control.

In order to more directly show the MWLAs fabricated by diameter modulation, the fluorescence microscopic images below and above the threshold of microdisks with diameters ranging from 8 to 20 μm are shown in **Figure 5**a, and the corresponding normalized lasing spectra of microdisks are shown in Figure 5b. The laser emission from different channels of the MWLA can be dynamically tuned over a large spectral range from 455 to 503 nm. The spectral coverage is ≈48 nm, equivalent to ≈63 THz in frequency, which is intrinsically limited by the gain bandwidth of the InGaN MQWs. As the fluorescence images displayed, the emission color of the microdisk above the threshold gradually transforms from green to blue with decreasing diametric dimensions. The detailed lasing wavelength and threshold energy density for different channels of the MWLA are summarized in Figure 5c, exhibiting a negative correlation between them. The MWLA in this study can be realized through only one epitaxial wafer and a single round of wafer bonding, which avoids the growth of multiple gain materials with different gain profiles as well as complex fabrication processes.

The strategy of fabricating MWLA through loss modulation is universal when microcavity with a broadband tunable material gain. We also realized MWLA on Si(100) by fabricating the microdisks with various cavity shapes. The theoretical Q factor of a polygonal microdisk with m-sides has been studied in previous studies.[41] With the same circumscribed circle diameter, increasing the number of sides m of a polygonal microdisk will increase the Q factor. Increasing m makes the shape of the microdisk closer to that of a circle, reducing the possibility of light scattering and leakage, and thus reducing energy loss. To verify the feasibility of this scheme, the microdisks with circular ($m = \infty$), orthohexagonal ($m = 6$), and quadrate ($m = 4$) morphologies were fabricated with the same outer tangent circle of 20 μm. The normalized lasing spectra and luminescence images of the respective cavities are shown in **Figure 6**a. The lasing wavelengths of the quadrate, orthohexagonal, and circular cavities are 459, 482, and 503 nm, respectively, and the corresponding color extends from blue to green. Such phenomena can be well elucidated by the proposed theoretical model involving the material gain shift and cavity loss modulation. Figure 6b shows the output intensity as a function of pumping energy for microdisks with different shapes. The spontaneous coupling factors β of the three microdisks were estimated to be 0.007, 0.008, and 0.018, respectively. A larger β indicates that more spontaneous photons can be incorporated into the lasing mode, thus reducing the threshold energy.[42] The statistical lasing thresholds and peak wavelengths for the respective cavity shapes are shown in Figure 6c,d, respectively. The thresholds of the circular microdisks are significantly lower and the lasing wavelengths are longer compared to those of the orthohexagonal and quadrate microdisks, with much more uniform intensity distribution. The significant data fluctuations observed in the orthohexagonal and quadrate microdisks can be attributed to fabrica-

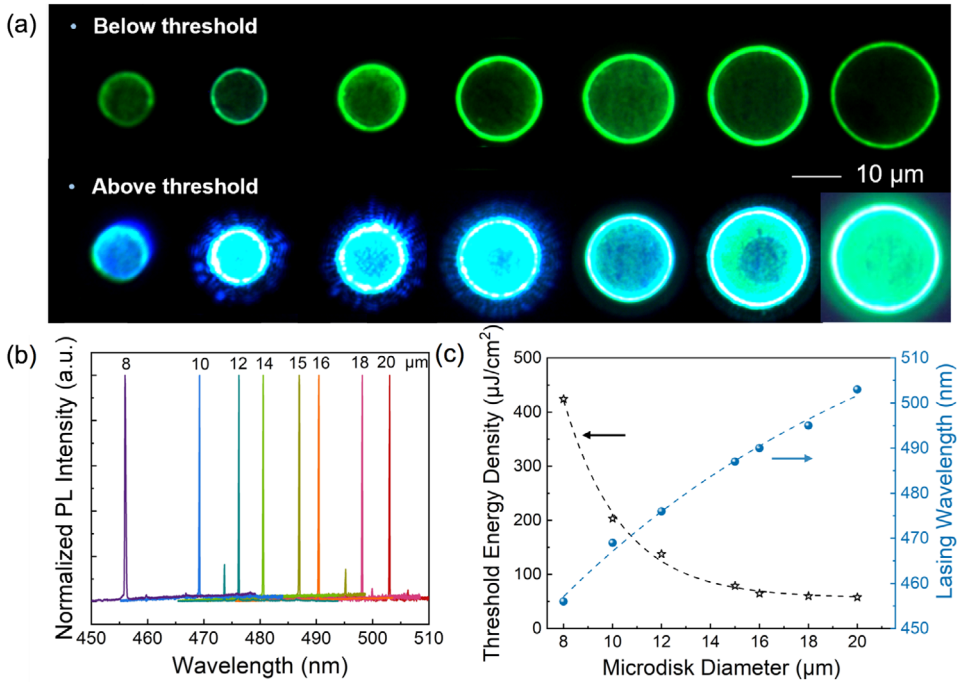

Figure 5. a) Microscopic images before (top) and after (bottom) lasing for circular microdisks with a diameter of 8–20 μm. b) Normalized PL spectra after lasing for circular microdisks of different sizes. c) Summary of lasing thresholds and lasing wavelengths for GaN-based circular microdisks with different diameters.

tion non-uniformities and variations in lithography precision at the sidewall intersections during the device manufacturing process. To investigate the mode leakage of microdisks with different shapes, the finite element method (FEM) was used to simulate the electric field of distributions |E| of optical modes inside the three cavities. Considering the limitations in lithography conditions, the actual fabricated devices exhibit boundary rounding effects at the intersections between sidewalls.[43] The simulated shapes were designed to match the rounding conditions of the fabricated devices, and the ideal mode field distributions for different cavity shapes are shown in Figure 6e. The Q factors of the circular, orthohexagonal, and quadrate microdisks were derived from the simulations as 4.9×10^4, 4×10^4, and 2.9×10^4, respectively. Since the simulation is an ideal case that does not consider the imperfect device shape and the sidewall roughness that is inevitable during the actual device manufacturing process,[44] the estimated Q factors are much larger than the actual value. However the variation tendency of the Q factor consists well with the experimental lasing characteristics of the three kinds of devices. Square and hexagonal-type microcavities with different sizes were also fabricated to study the size-dependent lasing tunability of a polygonal microcavity (Section S3, Supporting Information). However, due to the significantly higher optical losses in square and regular hexagonal cavities compared to circular devices, lasing is difficult when the cavity size is reduced below 20 μm. In future work, cavities with increased side numbers, approaching a circular geometry can be fabricated. Such resonant cavities exhibit lower losses and could facilitate the investigation of size-dependent lasing characteristics in polygonal microcavities.

3. Conclusion

In summary, a new theoretic model and fabrication method are proposed in this study to realize on-chip broadband GaN-based microdisk MWLAs on Si(100). High-quality green microdisk lasers with Q up to 13 138 and threshold as low as 57.85 μJ cm^{-2} at room temperature were demonstrated. The influence of the size and/or shape of the microdisk on the lasing wavelength was systematically investigated. By adjusting the cavity loss, we realized heterogeneous integration of MWLAs in a large spectral range from 456 to 503 nm. The fabrication method in this study avoids the complexity and high cost of existing technology and offers new possibilities and directions for ultra-high bandwidth integrated optics.

4. Experimental Section

The epitaxial wafer used in this work was grown on (0001)-oriented sapphire substrate by metal–organic chemical vapor deposition (MOCVD). First, a 2-μm thick unintentionally doped GaN layer and a 2-μm thick n-GaN were grown on a sapphire substrate, followed by 300-nm thick superlattice layers (SLs) and active region containing eight pairs of $In_{0.28}GaN/GaN$ (3 nm/15 nm) multi-quantum wells (MQWs). A 10 nm AlGaN electron-blocking layer (EBL) and a 100 nm thick p-GaN were sequentially grown. The fabrication process of the microdisk laser array is illustrated in Figure 1a. A SiO_2 layer was first deposited on the surface of the epi-wafer, and holes were opened in the SiO_2 (Step 1). Then the wafer was transferred to Si(100) substrate by flip-chip adhesive bonding (Step 2). In this step, the circular holes would be filled with the bonding material, which will act as the supporting pillar of the microdisks after device fabrication. The sapphire substrate was removed by laser lift-off (LLO) and

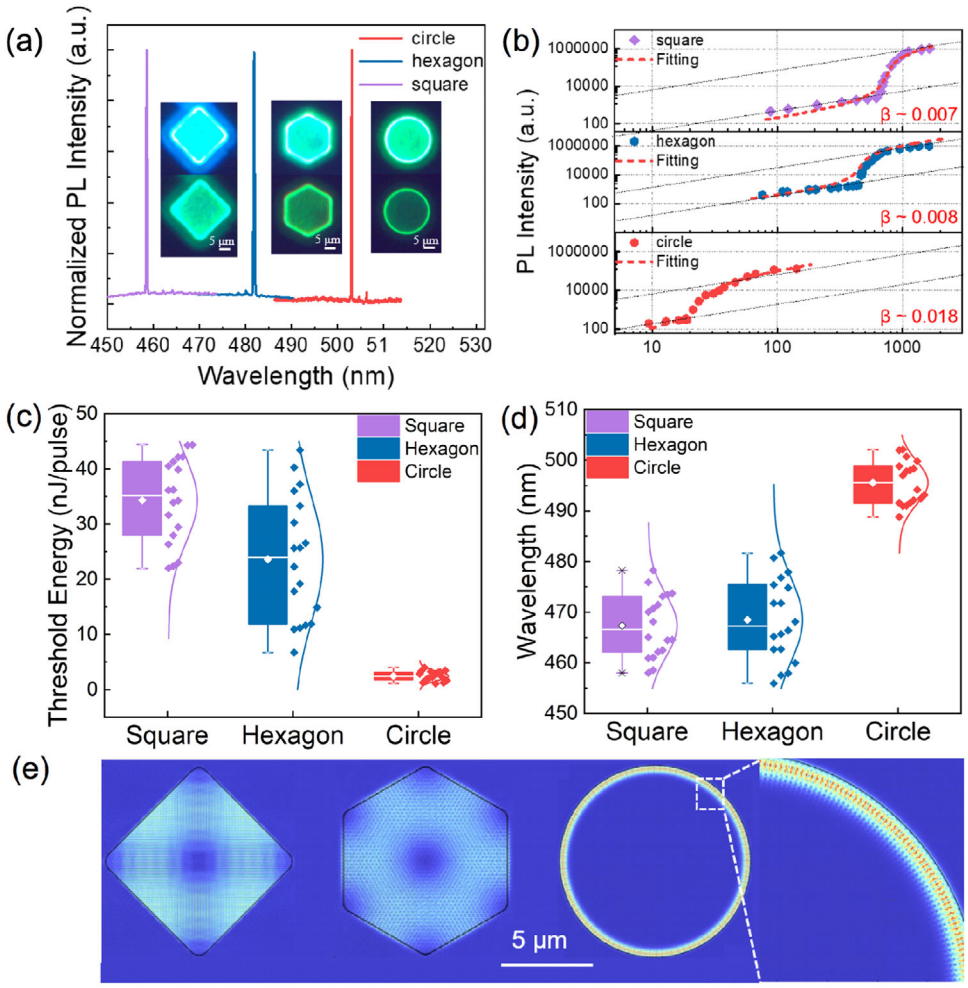

Figure 6. a) Normalized lasing spectra of microdisks with different geometric shapes. The inserts show the luminescence of each microdisk before and after lasing. b) Double-logarithmic integrated emission intensities versus pump energy for the microdisks with different geometries. c) Statistical box diagram of lasing threshold energies for microdisks with different geometric shapes. (The red horizontal line in the middle represents the data median line, and the semi-solid circle represents the average value.) d) Statistical box plots of lasing wavelengths of microdisks with different geometric shapes. e) Electric field distribution of the quadrate, orthohexagonal and circular microdisks, respectively, simulated by FEM.

the epitaxial film was thinned to 680 nm by CMP (Step 3). The microdisk arrays with different shapes and sizes were subsequently formed by inductively coupled plasma (ICP) etching, and the SiO_2 was exposed (Step 4). Finally, the SiO_2 sacrificial layer was removed by wet etching in HF solution, and the microdisk was supported by the photosensitive adhesive bonding material to form an air gap structure (Step 5).

Supporting Information

Supporting Information is available from the Wiley Online Library or from the author.

Acknowledgements

This work was supported by the National Natural Science Foundation of China (62474150, 62234011, 62104204, 62474067, U21A20493); Open Research Fund of State Key Laboratory of Materials for Integrated Circuits (No. SKLJC-K2024-08). L.M. and Y.M. conceived the concept, fabricated the devices, performed the data measurements and analysis, and wrote the initial manuscript; H.Z. and Z.S. participated in data analysis and experimental measurement; T.Y. participated in manuscript writing and data analysis; B.Z., G.W., S.C., L.Y. oversaw the entire project, and revised the manuscript. All authors participated in the manuscript discussion.

Conflict of Interest

The authors declare no conflict of interest.

Data Availability Statement

The data that support the findings of this study are available on request from the corresponding author. The data are not publicly available due to privacy or ethical restrictions.

Keywords

GaN, heterogeneous integration, microlaser arrays, multiwavelength

Received: January 20, 2025
Revised: March 7, 2025
Published online:

[1] Z. P. Zhou, B. Yin, J. Michel, *Light-Sci. Appl.* **2016**, *5*, 16098.
[2] C. Shang, Y. T. Wan, J. Selvidge, E. Hughes, R. Herrick, K. Mukherjee, J. A. Duan, F. Grillot, W. W. Chow, J. E. Bowers, *ACS Photonics* **2021**, *8*, 2555.
[3] a) C. W. He, W. Ali, *Photonics* **2023**, *10*, 1277; b) M. Dong, G. Clark, A. J. Leenheer, M. Zimmermann, D. Dominguez, A. J. Menssen, D. Heim, G. Gilbert, D. Englund, M. Eichenfield, *Nat. Photonics* **2022**, *16*, 59.
[4] J. K. Doylend, presented at Conf.Silicon Photonics XV, San Francisco, CA, **2020**.
[5] X. Y. Lu, Y. Sun, A. Chanana, U. A. Javid, M. Davanco, K. Srinivasan, *Photonics Res.* **2023**, *11*, 500375.
[6] D. T. Spencer, T. Drake, T. C. Briles, J. Stone, L. C. Sinclair, C. Fredrick, Q. Li, D. Westly, B. R. Ilic, A. Bluestone, N. Volet, T. Komljenovic, L. Chang, S. H. Lee, D. Y. Oh, M. G. Suh, K. Y. Yang, M. H. P. Pfeiffer, T. J. Kippenberg, E. Norberg, L. Theogarajan, K. Vahala, N. R. Newbury, K. Srinivasan, J. E. Bowers, S. A. Diddams, S. B. Papp, *Nature* **2018**, *557*, 81.
[7] a) N. L. Kazanskiy, S. N. Khonina, M. A. Butt, *Photonics* **2022**, *9*, 331; b) Z. Xiao, W. X. Liu, S. Y. Xu, J. K. Zhou, Z. H. Ren, C. K. Lee, *Adv. Opt. Mater.* **2023**, *11*, 2301028.
[8] a) N. von den Driesch, D. Stange, D. Rainko, I. Povstugar, P. Zaumseil, G. Capellini, T. Schröder, T. Denneulin, Z. Ikonic, J. M. Hartmann, H. Sigg, S. Mantl, D. Grützmacher, D. Buca, *Adv. Sci.* **2018**, *5*, 1700955; b) S. Wirths, R. Geiger, N. von den Driesch, G. Mussler, T. Stoica, S. Mantl, Z. Ikonic, M. Luysberg, S. Chiussi, J. M. Hartmann, H. Sigg, J. Faist, D. Buca, D. Grützmacher, *Nat. Photonics* **2015**, *9*, 88.
[9] H. S. Rong, A. S. Liu, R. Jones, O. Cohen, D. Hak, R. Nicolaescu, A. Fang, M. Paniccia, *Nature* **2005**, *433*, 03273.
[10] D. Liang, G. Roelkens, R. Baets, J. E. Bowers, *Materials* **2010**, *3*, 1782.
[11] a) X. F. Zhang, Z. C. Li, Y. Y. Zhang, X. D. Wang, X. Y. Yi, G. H. Wang, J. M. Li, *Opt. Express* **2022**, *30*, 462422; b) Y. Han, H. Park, J. Bowers, K. M. Lau, *Adv.Opt.Photonics* **2022**, *14*, 455976.
[12] a) W. Q. Wei, A. He, B. Yang, Z. H. Wang, J. Z. Huang, D. Han, M. Ming, X. H. Guo, Y. K. Su, J. J. Zhang, T. Wang, *Light-Sci. Appl.* **2023**, *12*, 84; b) W. Q. Wei, presented at Conf.Asia Communications and Photonics Conference (ACP)/ International Conference on Information Photonics and Optical Communications (IPOC), Shenzhen, **2022**.
[13] R. Helkey, A. A. M. Saleh, J. Buckwalter, J. E. Bowers, *IEEE J. Selected Topics Quant. Electron.* **2019**, *25*, 2903775.
[14] X. F. Chen, W. Liu, J. M. An, Y. Liu, K. Xu, X. Wang, J. G. Liu, Y. F. Ji, N. H. Zhu, *Chin. Sci. Bull.* **2011**, *56*, 11434.
[15] C. Zhang, S. J. Zhang, J. D. Peters, J. E. Bowers, *Optica* **2016**, *3*, 785.
[16] Z. Su, R. Xiao, Z. Sun, Z. Yang, Y. Du, Z. Chen, J. Zheng, Y. Zhang, J. Lu, Y. Shi, (preprint)arXiv **2020**, 01178v1.
[17] H. J. Yu, presented at Conf. Optical Fiber Communications Conference and Exhibition (OFC), San Diego, CA, **2022**.
[18] a) F. Tabataba-Vakili, L. Doyennette, C. Brimont, T. Guillet, S. Rennesson, E. Frayssinet, B. Damilano, J. Y. Duboz, F. Semond, I. Roland, M. El Kurdi, X. Checoury, S. Sauvage, B. Gayral, P. Boucaud, *ACS Photonics* **2018**, *5*, 3643; b) J. Ward, O. Benson, *Laser Photon. Rev.* **2011**, *5*, 201000025.
[19] a) S. S. Sui, M. Y. Tang, Y. D. Yang, J. L. Xiao, Y. Du, Y. Z. Huang, *IEEE J. Quantum Electron.* **2015**, *51*, 2600108; b) J. Van Campenhout, L. Liu, P. R. Romeo, D. Van Thourhout, C. Seassal, P. Regreny, L. Di Cioccio, J. M. Fedeli, R. Baets, *IEEE Photonics Technol. Lett.* **2008**, *20*, 1345; c) D. Liang, A. Roshan-Zamir, Y. H. Fan, C. Zhang, B. H. Wang, A. Descos, W. Q. Shen, K. Z. Yu, C. Li, G. F. Fan, G. Kurczveil, Y. T. Hu, Z. H. Huang, M. Fiorentino, S. Kumar, S. M. Palermo, R. G. Beausoleil, *J. Lightwave Technol.* **2020**, *38*, 2959048.
[20] a) P. Serra, A. Piqué, *Adv. Mater. Technol.* **2019**, *4*, 1800099; b) Y. Lin, W. W. Qian, H. Z. Li, H. L. Ma, Z. H. Jin, *Opt. Commun.* **2021**, *491*, 126954.
[21] Y. D. Lin, Z. Yong, X. S. Luo, S. S. Azadeh, J. C. Mikkelsen, A. Sharma, H. Chen, J. C. C. Mak, P. G. Q. Lo, W. D. Sacher, J. K. S. Poon, *Nat. Commun.* **2022**, *13*, 6362.
[22] a) S. Jooken, K. Zinoviev, G. Yurtsever, A. De Proft, K. de Wijs, Z. Jafari, A. Lebanov, G. Jeevanandam, M. Kotyrba, E. Gorjup, J. Fondu, L. Lagae, S. Libbrecht, P. Van Dorpe, N. Verellen, *Sci. Rep.* **2024**, *14*, 10921; b) A. Z. Subramanian, E. Ryckeboer, A. Dhakal, F. Peyskens, A. Malik, B. Kuyken, H. L. Zhao, S. Pathak, A. Ruocco, A. De Groote, P. Wuytens, D. Martens, F. Leo, W. Q. Xie, U. D. Dave, M. Muneeb, P. Van Dorpe, J. Van Campenhout, W. Bogaerts, P. Bienstman, N. Le Thomas, D. Van Thourhout, Z. Hens, G. Roelkens, R. Baets, *Photonics Res.* **2015**, *3*, 047.
[23] a) A. Mohanty, Q. Li, M. A. Tadayon, S. P. Roberts, G. R. Bhatt, E. Shim, X. C. Ji, J. Cardenas, S. A. Miller, A. Kepecs, M. Lipson, *Nat. Biomed. Eng.* **2020**, *4*, 223; b) L. C. Moreaux, D. Yatsenko, W. D. Sacher, J. Choi, C. Lee, N. J. Kubat, R. J. Cotton, E. S. Boyden, M. Z. Lin, L. Tian, A. S. Tolias, J. K. S. Poon, K. L. Shepard, M. L. Roukes, *Neuron* **2020**, *108*, 66.
[24] X. K. Tang, L. Zhang, C. M. Sun, Z. Chen, H. J. Wang, R. Jiang, Z. Y. Li, W. Shi, A. D. Zhang, *IEEE Access* **2020**, *8*, 3037174.
[25] M. C. Shin, A. Mohanty, K. Watson, G. R. Bhatt, C. T. Phare, S. A. Miller, M. Zadka, B. S. Lee, X. C. Ji, I. Datta, M. Lipson, *Opt. Lett.* **2020**, *45*, 385201.
[26] J. Xiong, E.-L. Hsiang, Z. He, T. Zhan, S.-T. Wu, **2021**, *10*.
[27] W. W. Bi, H. H. Kuo, P. Ku, B. Shen, *Handbook of GaN semiconductor materials and devices*, CRC Press, Boca Raton, FL **2017**.
[28] Y. Sun, K. Zhou, Q. Sun, J. P. Liu, M. X. Feng, Z. C. Li, Y. Zhou, L. Q. Zhang, D. Y. Li, S. M. Zhang, M. Ikeda, S. Liu, H. Yang, *Nat. Photonics* **2016**, *10*, 158.
[29] Y. J. Tang, M. X. Feng, J. X. Liu, X. J. Sun, S. M. Yan, S. Z. Fan, Q. Sun, S. M. Zhang, M. Ikeda, H. Yang, *J. Phys. D-Appl. Phys.* **2022**, *55*, 195103.
[30] Y. T. Hu, D. Liang, K. Mukherjee, Y. L. Li, C. Zhang, G. Kurczveil, X. Huang, R. G. Beausoleil, *Light-Sci. Appl.* **2019**, *8*, 93.
[31] H. C. Yu, Z. W. Zheng, Y. Mei, R. B. Xu, J. P. Liu, H. Yang, B. P. Zhang, T. C. Lu, H. C. Kuo, *Prog. Quantum Electron.* **2018**, *57*, 001.
[32] a) Y. Mei, M. C. Xie, H. Long, L. Y. Ying, B. P. Zhang, *J. Lightwave Technol.* **2022**, *40*, 3147803; b) M. X. Feng, H. R. Zhao, R. Zhou, Y. J. Tang, J. X. Liu, X. J. Sun, Q. Sun, H. Yang, *ACS Photonics* **2022**, *10*, 2c01046.
[33] J. Heo, W. Guo, P. Bhattacharya, *Appl. Phys. Lett.* **2011**, *98*, 021110.
[34] a) J. H. Ryou, P. D. Yoder, J. P. Liu, Z. Lochner, H. Kim, S. Choi, H. J. Kim, R. D. Dupuis, *IEEE J. Sel. Top. Quantum Electron.* **2009**, *15*, 2014170; b) B. Arnaudov, D. S. Domanevskii, S. Evtimova, C. Ivanov, R. Kakanakov, *Microelectron. J.* **2009**, *40*, 064.
[35] Z. F. Zhang, P. Miao, J. B. Sun, S. Longhi, N. M. Litchinitser, L. Feng, *ACS Photonics* **2018**, *5*, 8b00800.
[36] W. Y. Fu, Y. F. Cheung, H. W. Choi, *Opt. Lett.* **2022**, *47*, 479375.
[37] G. E. Weng, J. Y. Yan, S. J. Chen, C. H. Zhao, H. B. Zhang, J. Tian, Y. J. Liu, X. B. Hu, J. H. Tao, S. Q. Chen, Z. Q. Zhu, H. Akiyama, J. H. Chu, *Photonics Res.* **2021**, *9*, 409884.
[38] a) R. E. Slusher, A. F. J. Levi, U. Mohideen, S. L. McCall, S. J. Pearton, R. A. Logan, *Appl. Phys. Lett.* **1993**, *63*, 109714; b) I. Rousseau, G. Callsen, G. Jacopin, J. F. Carlin, R. Butté, N. Grandjean, *J. Appl. Phys.* **2018**, *123*, 113103.

[39] M. Borselli, T. J. Johnson, O. Painter, *Opt. Express* **2005**, *13*, 001515.
[40] A. E. Zhukov, E. I. Moiseev, A. M. Nadtochiy, N. A. Fominykh, K. A. Ivanov, I. S. Makhov, M. V. Maximov, F. I. Zubov, V. G. Dubrovskii, S. A. Mintairov, N. A. Kalyuzhnyy, N. Y. Gordeev, Y. M. Shernyakov, N. V. Kryzhanovskaya, *IEEE J. Quantum Electron.* **2023**, *59*, 2000108.
[41] a) X. Y. Tian, L. Wang, W. Li, Q. Q. Lin, Q. Cao, *ACS Appl. Mater. Interfaces* **2021**, *13*, 0c21824; b) M. H. Liu, P. Chen, J. Zhou, R. Xu, X. K. Mao, Z. L. Xie, X. Q. Xiu, D. J. Chen, B. Liu, P. Han, Y. Shi, R. Zhang, Y. D. Zheng, K. Cheng, L. Y. Zhang, *J. Appl. Phys.* **2020**, *127*, 113102.
[42] Y. Yamamoto, S. Machida, G. Bjork, *Phys. Rev. A* **1991**, *44*, 657.
[43] J. Wiersig, *Phys. Rev. A* **2003**, *67*, 023807.
[44] a) C. Li, L. J. Zhou, S. M. Zheng, A. W. Poon, *IEEE J. Sel. Top. Quantum Electron.* **2006**, *12*, 883150; b) H. Kudo, R. Suzuki, T. Tanabe, *Phys. Rev. A* **2013**, *88*, 023807.